A&A 664, A119 (2022)
https://doi.org/10.1051/0004-6361/202243422

Astronomy & Astrophysics

Deuteration of c-C_3H_2 towards the pre-stellar core L1544

K. Giers[1], S. Spezzano[1], F. Alves[1], P. Caselli[1], E. Redaelli[1], O. Sipilä[1], M. Ben Khalifa[2], L. Wiesenfeld[3], S. Brünken[4], and L. Bizzocchi[5,6]

[1] Max Planck Institute for Extraterrestrial Physics, Giessenbachstrasse 1, 85748 Garching, Germany
e-mail: kgiers@mpe.mpg.de
[2] KU Leuven, Department of Chemistry, Celestijnenlaan 200F, 3001 Leuven, Belgium
[3] Laboratoire Aimé-Cotton, Bâtiment 505, CNRS, Université Paris-Saclay, 91405 Orsay, France
[4] Radboud University, Institute for Molecules and Materials, FELIX Laboratory, Toernooiveld 7, 6525ED Nijmegen, The Netherlands
[5] Scuola Normale Superiore, Piazza dei Cavalieri 7, 56126 Pisa, Italy
[6] Dipartimento di Chimica "Giacomo Ciamician", Università di Bologna, Via Selmi 2, 40126 Bologna, Italy

Received 25 February 2022 / Accepted 24 May 2022

ABSTRACT

Context. In the centre of pre-stellar cores, the deuterium fractionation is enhanced due to the cold temperatures and high densities. Therefore, the chemistry of deuterated molecules can be used to probe the evolution and the kinematics in the earliest stages of star formation.
Aims. We analyse emission maps of cyclopropenylidene, c-C_3H_2, to study the distribution of the deuteration throughout the prototypical pre-stellar core L1544.
Methods. We used single-dish observations of c-C_3H_2, c-$H^{13}CC_2H$, c-C_3HD, and c-C_3D_2 towards the pre-stellar core L1544, performed at the IRAM 30 m telescope. We derived the column density and deuterium fraction maps, and compared these observations with non-local thermodynamic equilibrium radiative transfer simulations.
Results. The highest deuterium fractions are found close to the dust peak at the centre of L1544, where the increased abundance of H_2D^+ ions drives the deuteration process. The peak values are N(c-C_3HD)/N(c-C_3H_2) = 0.17 ± 0.01, N(c-C_3D_2)/N(c-C_3H_2) = 0.025 ± 0.003, and N(c-C_3D_2)/N(c-C_3HD) = 0.16 ± 0.03, which is consistent with previous single-pointing observations. The distributions of c-C_3HD and c-C_3D_2 indicate that the deuterated forms of c-C_3H_2 in fact trace the dust peak and not the c-C_3H_2 peak.
Conclusions. The N(c-C_3D_2)/N(c-C_3HD) map confirms that the process of deuteration is more efficient towards the centre of the core and demonstrates that carbon-chain molecules are still present at high densities. This is likely caused by an increased abundance of He^+ ions destroying CO, which increases the number of carbon atoms in the gas phase.

Key words. astrochemistry – ISM: clouds – ISM: molecules – ISM: abundances – stars: formation – ISM: individual objects: L1544

1. Introduction

Pre-stellar cores represent the initial conditions of low-mass star formation. The self-gravitating cores (Ward-Thompson et al. 1999) are dense ($n > 10^5$ cm^{-3}) and cold ($T < 10$ K) towards their centre (Crapsi et al. 2007; Caselli et al. 2012), showing signs of contraction motion and chemical evolution (Crapsi et al. 2005). Therefore, pre-stellar cores are ideal laboratories for studying the physical and chemical processes taking place in the early stages of low-mass star formation.

In the cold and dense conditions of pre-stellar cores, the deuteration of molecules is a favoured chemical process (Ceccarelli et al. 2014), which increases the abundance of deuterated species. The deuterium fractionation is driven by the gas-phase reaction (only true with respect to para-states of reactants and products; Pagani et al. 1992)

$$H_3^+ + HD \rightleftharpoons H_2D^+ + H_2 + 232\,\mathrm{K}. \quad (1)$$

This reaction is exothermic. As the temperature decreases, the abundance of H_2D^+ ions is enhanced, which drives the deuteration of other molecules. Because the reaction is more efficient from left to right at low temperatures, H_2D^+ is no longer destroyed when it meets an H_2 molecule, but is mostly destroyed by CO. However, in cold and dense regions such as pre-stellar cores, CO is highly depleted from the gas phase and frozen out onto dust grains (Willacy et al. 1998; Caselli et al. 1999; Bacmann et al. 2003; Crapsi et al. 2005), which further increases the deuterium fractionation (Dalgarno & Lepp 1984). The para-H_2D^+ is further deuterated by successive reactions with HD, leading to noticeable densities of both D_2H^+ and D_3^+ (Hily-Blant et al. 2018; Caselli et al. 2019). All three deuterium-substituted H_3^+ ions drive the deuteration of other molecules by transfer of a D^+ atom. Furthermore, the level of deuteration also depends on the ortho-to-para ratio of H_2. The higher the ratio, the more H_2D^+ is destroyed by ortho-H_2 because the energy of the ground state of ortho-H_2 compared to para-H_2, ~170 K, is close to the exothermicity of reaction (1). However, the ortho-to-para ratio of H_2 in pre-stellar cores is usually $\sim 10^{-3}$ (Kong et al. 2015), further promoting the deuterium fractionation. Deuterated molecules hence have proven to be very good tracers of the central parts of dense cores that are on the verge of star formation (Crapsi et al. 2007; Redaelli et al. 2019) because a large deuterium enrichment is characteristic for these high-density nuclei (Crapsi et al. 2005). The deuterium fraction is measured by the ratio $R_{D/H}$ of the molecular tracer, dividing the column density of the D-bearing molecule by the column density of the hydrogenated

Table 1. Observed lines and observation details.

Molecule	Transition ($J'_{K'_a K'_c} - J_{K_a K_c}$)	Frequency [a] (GHz)	rms (mK)	*HPBW* ($''$)	$F_{\rm eff}/B_{\rm eff}$	Velocity range [b] (km s^{-1})	Reference
c-C_3H_2	$3_{22}-3_{13}$	84.728	22	30.6	0.95/0.838	6.90−7.42	1
c-H^{13}CC$_2$H	$2_{12}-1_{01}$	84.186	22	30.8	0.95/0.839	6.83−7.35	2
c-C_3HD	$3_{03}-2_{12}$	104.187	27	24.9	0.95/0.802	6.78−7.48	2
c-C_3D_2	$3_{13}-2_{02}$	97.762	21	26.5	0.95/0.814	6.89−7.49	3

Notes. [a]Extracted from Cologne database for molecular spectroscopy (Müller et al. 2001). [b]Velocity ranges where the integrated emission has been computed.
References. (1) Thaddeus et al. (1985); (2) Bogey et al. (1987); (3) Spezzano et al. (2012).

isotopologue. In addition, the level of deuteration is sensitive to the evolutionary stage of starless cores (Crapsi et al. 2005; Chantzos et al. 2018). Therefore, it can work as a chemical clock and can be used as a diagnostic tool.

Cyclopropenylidene (c-C_3H_2) is one of the most abundant and widespread molecules in the Galaxy. Its first detection in space was made by Thaddeus et al. (1981), which was later confirmed by the first laboratory detection by Thaddeus et al. (1985). Since then, c-C_3H_2 has been observed in diffuse gas, cold dark clouds, giant molecular clouds, photodissociation regions, circumstellar envelopes, planetary nebulae, circumstellar disks, and low-mass protostars (Thaddeus et al. 1985; Matthews & Irvine 1985; Seaquist & Bell 1986; Vrtilek et al. 1987; Cox et al. 1987; Madden et al. 1989; Lucas & Liszt 2000; Teyssier et al. 2005; Qi et al. 2013; Majumdar et al. 2017). As the formation of c-C_3H_2 is believed to occur solely in the gas phase (Park et al. 2006), it preferentially traces dense and chemically young gas, which is gas where the C atoms have not yet been mainly locked into CO (Spezzano et al. 2016). However, it also suffers from depletion, and therefore it does not trace the central regions of pre-stellar cores but more external layers (Spezzano et al. 2017). Following the detection of its singly and doubly deuterated isotopologues (Gerin et al. 1987; Spezzano et al. 2013), c-C_3H_2 is a unique probe for studying the deuteration processes that take place in the gas phase in pre-stellar cores because it is only efficiently deuterated there (Spezzano et al. 2013).

The low-mass pre-stellar core L1544 is located in the Taurus molecular cloud complex, one of the nearest star-forming regions, at a distance of 170 pc (Galli et al. 2019). The dense core is a well-known object; numerous and extensive studies have led to a profound knowledge of its physical and chemical structure (Crapsi et al. 2007; Keto et al. 2004, 2015; Keto & Caselli 2010; Caselli et al. 2002a). It is centrally concentrated (Ward-Thompson et al. 1999), with a high central density of around 10^6 cm^{-3} within the central 2000 AU (Crapsi et al. 2007; Caselli et al. 2019), and it is very cold, with a temperature ranging from 12 K in the outskirts down to ∼6 K towards the centre (Crapsi et al. 2007). The core has an elongated shape and shows signs of contraction, suggesting that it is on the verge of gravitational collapse (Williams et al. 1999; Ohashi et al. 1999; Lee et al. 2001; Caselli et al. 2002a, 2012). Towards its centre, L1544 exhibits a high degree of CO freeze-out (93%; Caselli et al. 2002a; Crapsi et al. 2005) and a high level of deuteration (Crapsi et al. 2005; Redaelli et al. 2019). It is chemically rich, showing spatial inhomogeneities in the distribution of molecular emission (Spezzano et al. 2017; Redaelli et al. 2019; Chacón-Tanarro et al. 2019).

In this work we present emission maps of c-C_3H_2, the singly and doubly deuterated isotopologues, c-C_3HD and c-C_3D_2, as well as the isotopologue c-H^{13}CC$_2$H towards L1544. In Sect. 2 we describe the observations, followed by the results in Sect. 3. The analysis in Sect. 4 is divided into the derivation of the c-C_3H_2 deuteration maps and a comparison of the dust emission peak column density with non-local thermodynamic equilibrium (non-LTE) simulations. We discuss the results in Sect. 5 and present our conclusions in Sect. 6.

2. Observations

The emission maps presented in this paper were obtained using the IRAM 30 m single-dish telescope located in Pico Veleta, Spain, in October 2013. The observed $2.5' \times 2.5'$ on-the-fly (OTF) maps are centred on the source dust emission peak (α_{2000} = 05$^{\rm h}$04$^{\rm m}$17$^{\rm s}$.21, δ_{2000} = +25°10′42″.8, Ward-Thompson et al. 1999). We applied position switching, with the reference position set at (−180″,180″) offset with respect to the map centre. The EMIR E090 receiver was used along with the Fourier transform spectrometer backend (FTS), with a spectral resolution of 50 kHz. The antenna moved along an orthogonal pattern of linear paths separated by 8″ intervals, corresponding roughly to one-third of the beam full width at half maximum (FWHM). The weather conditions during the mapping were good ($\tau \sim 0.03$), with a typical system temperature of $T_{\rm sys} \sim 90-100$ K.

The observed transitions are summarised in Table 1. Figure 1 shows the corresponding integrated intensity maps for each molecule. The data were processed using the GILDAS software (Pety 2005) and Python. All emission maps were gridded to a pixel size of 8″ with the CLASS software in the GILDAS packages; this corresponds to one-third to one-quarter of the actual beam size, depending on the frequency. The antenna temperature T_A^* was converted into the main-beam temperature $T_{\rm mb}$ using the relation $T_{\rm mb} = F_{\rm eff}/B_{\rm eff} \cdot T_A^*$. The corresponding values for the 30 m forward ($F_{\rm eff}$) and main-beam efficiency ($B_{\rm eff}$) ratios are given in Table 1.

3. Results

The integrated intensities were derived calculating the zeroth moment of the emission maps, integrating over the velocity ranges given in Table 1. The ranges contain all velocity channels whose map showed a signal-to-noise ratio higher than or equal to 3. To enable the comparison between the molecules, all maps were convolved to an angular resolution of 31″, which corresponds to the half-power beam width (HPBW) of the largest observed beam (c-H^{13}CC$_2$H$_2$).

c-C_3H_2. The integrated intensity map of para-c-C_3H_2 ($3_{22}-3_{13}$) is shown in the top left panel of Fig. 1. The emission peak is located south-east of the dust peak. This is driven by a non-uniform illumination from the interstellar radiation

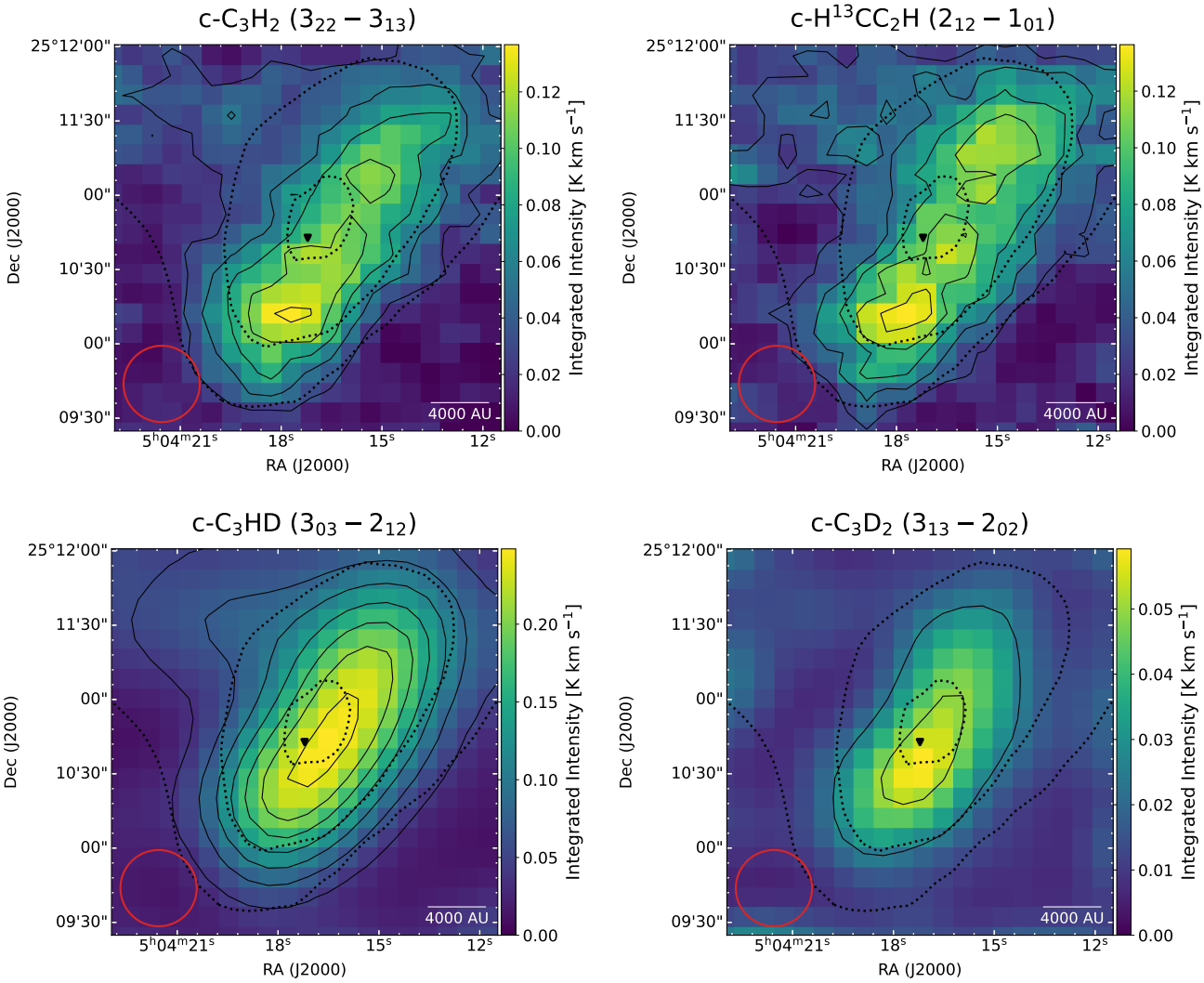

Fig. 1. Integrated intensity maps of the observed transitions. The dashed black lines represent 90, 50, and 30% of the H_2 column density peak value derived from *Herschel* maps (Spezzano et al. 2016), 2.8×10^{22} cm^{-2}. The solid lines represent contours of the integrated intensity starting at 3σ with steps of 3σ. *From top to bottom and left to right*, the average errors on the integrated intensity are 9, 9, 12, and 8 in units of mK km s^{-1}. The dust peak is indicated by the black triangle. The beam size of the 30 m telescope, $HPBW = 31''$, is shown by the red circle in the bottom left corner of each panel, and the scale bar is shown in the bottom right corners.

field, which dominates towards the southern part of the core and leads to more C atoms in the gas phase and subsequently, to an increased formation of c-C_3H_2, as discussed in Spezzano et al. (2016).

c-H^{13}CC$_2$H$_2$. The distribution of the c-H^{13}CC$_2$H$_2$ integrated emission (Fig. 1, top right panel) follows the distribution of c-C_3H_2, with an emission peak located at the c-C_3H_2 peak and similar values of integrated intensity.

c-C$_3$HD. The integrated intensity map of c-C_3HD, bottom left panel of Fig. 1, peaks in an elongated region passing through the dust peak, where temperature and density are suitable for the deuteration process to take place. The emission peak follows the direction of the major axis and extends more to the north-west than to the south-east, suggesting a flattened central structure, as predicted by simulations of magnetised core contraction (see e.g. Caselli et al. 2019).

c-C$_3$D$_2$. The integrated intensity map of c-C_3D_2 is shown in the bottom right panel of Fig. 1. The emission peak is located very close to the dust peak, confirming that the level of deuteration is higher closer to the centre of the core. In addition, the emission is less extended than for c-C_3H_2 and c-C_3HD. It probably traces a higher density and more central shell of the core.

4. Analysis

4.1. Column densities

We calculated all column densities using the assumption of optically thin emission, as presented in Mangum & Shirley (2015). Furthermore, we applied the approximation of a constant excitation temperature throughout the core (CTex), following Caselli et al. (2002b) and Redaelli et al. (2019),

$$N = \frac{8\pi\nu^3}{c^3} \frac{Q_{\rm rot}(T_{\rm ex})}{g_u A_{\rm ul}} \left[J_\nu(T_{\rm ex}) - J_\nu(T_{\rm bg})\right]^{-1} \frac{e^{\frac{E_u}{kT_{\rm ex}}}}{e^{\frac{h\nu}{kT_{\rm ex}}} - 1} \int T_{\rm mb} {\rm d}v, \quad (2)$$

Table 2. Parameters used in the derivation of the column densities.

Molecule	T_{ex} (K)	Q(T_{ex})	E_u (K)	A (10^{-5}s^{-1})	g_u
c-C_3H_2 (3_{22}–3_{13})	6	37.68	16.14	1.04	7
c-H^{13}CC_2H (2_{12}–1_{01})	6	38.69	6.33	2.17	10
c-C_3HD (3_{03}–2_{12})	5	50.10	10.86	3.96	21
c-C_3D_2 (3_{13}–2_{02})	5	86.37	9.89	3.88	42

Table 3. Properties of the spectral lines extracted at the dust peak and the c-C_3H_2 peak.

Molecule	T_{mb} (K)	τ [a]	rms (mK)	W (K km s^{-1})	v_{LSR} (km s^{-1})	Δv [b] (km s^{-1})	N [a] (10^{12} cm^{-2})
				Dust peak			
c-C_3H_2	0.28(4)	0.10(1)	35	0.10(2)	7.20(2)	0.33(5)	17(3)
c-H^{13}CC_2H	0.19(3)	0.07(1)	32	0.12(3)	7.15(4)	0.6(1)	1.3(3)
c-C_3HD	0.59(3)	0.36(2)	39	0.27(2)	7.20(1)	0.43(3)	5.3(4)
c-C_3D_2	0.14(2)	0.07(1)	27	0.07(2)	7.19(4)	0.47(9)	0.88(3)
				c-C_3H_2 peak			
c-C_3H_2	0.49(4)	0.18(1)	28	0.14(2)	7.21(1)	0.27(3)	23(3)
c-H^{13}CC_2H	0.32(3)	0.10(1)	32	0.13(2)	7.21(2)	0.40(4)	1.4(2)
c-C_3HD	0.74(4)	0.47(2)	39	0.24(2)	7.29(1)	0.31(2)	4.7(4)
c-C_3D_2	0.16(3)	0.08(2)	27	0.04(1)	7.30(2)	0.25(6)	0.5(1)

Notes. [a]Derived using the excitation temperatures listed in Table 2.[b]Observed line width.

where $Q_{rot}(T_{ex})$ is the partition function of the molecule at an excitation temperature T_{ex}, g_u and E_u are the degeneracy and energy of the upper level of the transition, respectively, A_{ul} is the Einstein coefficient for spontaneous emission, T_{bg} = 2.73 K is the temperature of the cosmic microwave background, $J(T)$ is the Rayleigh-Jeans equivalent temperature, and T_{mb} is the main-beam temperature. The corresponding parameters for each transition used in the derivation of the column density are listed in Table 2.

As excitation temperature, we used 6 K for the main species and for the ^{13}C-bearing isotopologue (see Gerin et al. 1987). For the deuterated isotopologues, we chose an excitation temperature of 5 K, following Spezzano et al. (2013). The effect of the excitation temperature on the derived column density ratios was found to be small, with a change of a few percent upon a variation of ±1 K (as stated in Spezzano et al. 2013).

Our assumption of a constant excitation temperature applied across the maps follows the analysis presented in the appendix of Redaelli et al. (2019). There, the authors proved that their results were not sensitive to the variations of the excitation temperature across the core, and thus the analysis can be carried out assuming a constant value. As our observations have similarly sized maps and angular resolution, we applied this assumption.

The derived column density maps are shown in Fig. A.1. The morphologies of the maps follow the integrated intensity maps shown in Fig. 1. The main species shows the highest column densities, peaking at 2.0×10^{13} cm^{-2}. The ^{13}C isotopologue and the singly deuterated form have a lower peak column density than the main isotopologue, with peak values around 1.3×10^{12} cm^{-2} and 4.0×10^{12} cm^{-2}. Furthermore, the doubly deuterated isotopologue only peaks at $\sim6.3\times10^{11}$ cm^{-2}, also one order of magnitude lower in column density than its precursor molecule, c-C_3HD. On average, the uncertainties on the column density maps are 1×10^{12} cm^{-2}, 9×10^{10} cm^{-2}, 2×10^{11} cm^{-2}, and 1×10^{11} cm^{-2} for c-C_3H_2, c-H^{13}CC_2H_2, c-C_3HD, and c-C_3D_2, respectively. The error maps were derived through standard error propagation from the rms maps, which were calculated from the velocity channel maps that do not show any signal.

Furthermore, we extracted spectra at the dust peak and the c-C_3H_2 peak of L1544. They are shown in Fig. B.1. Using Gaussian fitting in Python, we derived the column densities at the two peaks. The resulting best-fit parameters along with the corresponding column densities and optical depths are summarised in Table 3. In general, the derived column densities of the deuterated isotopologues are higher towards the dust peak than towards the c-C_3H_2 peak. The derived optical depths show that all observed lines are optically thin. However, by multiplying the column density of the ^{13}C isotopologue with the isotopic ratio for the local interstellar medium, ^{12}C/^{13}C = 68 (Milam et al. 2005), divided by two (to account for the degeneracy of c-H^{13}CC_2H regarding the position of the ^{13}C atom), we obtain an additional way to determine the column density of the main isotopologue. Despite the large uncertainty of the resulting value, N(^{13}C,CTex) = $(44\pm10)\times10^{12}$ cm^{-2}, it might suggest that the c-C_3H_2 (3_{33}–3_{13}) transition is moderately optically thick.

4.2. Deuterium fraction

The deuterium fraction maps were derived by dividing the column density maps of the deuterated isotopologues by that of the main species, pixel by pixel. To avoid issues with the optical depth of the main isotopologue, we used the column density map for c-C_3H_2 derived from the ^{13}C isotopologue multiplied by the isotopic ratio for the local interstellar medium divided by two, ^{12}C/^{13}C = 68/2 = 34. Colzi et al. (2020) showed that in the local interstellar medium, the ratio is molecule-dependent and varies with time, volume density, and temperature, and can deviate significantly from 68. For example, for a fixed density and temperature, it may change by a factor of 2 between 10^5 and

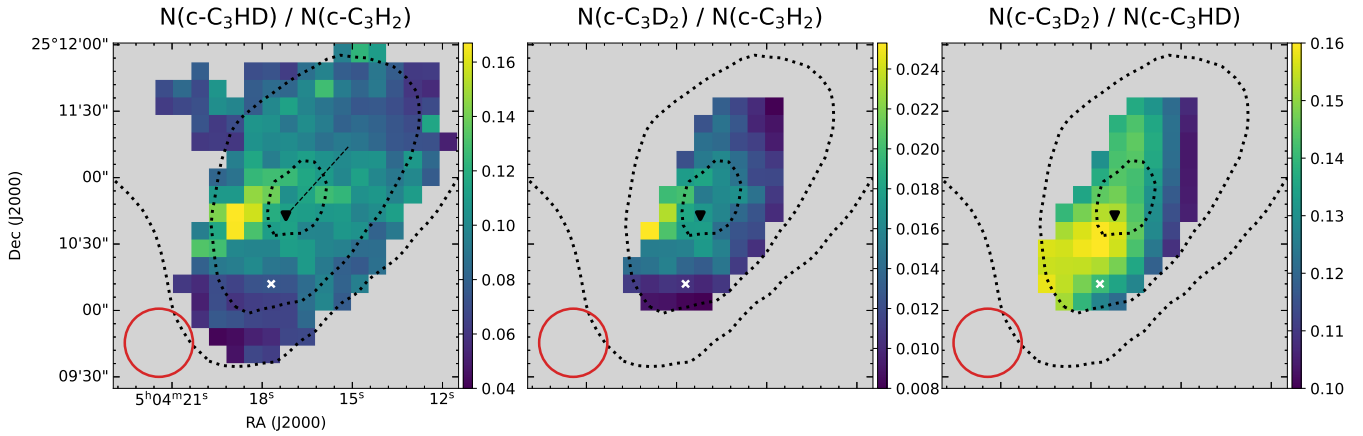

Fig. 2. Deuteration maps of c-C_3H_2. Only pixels above 3σ are plotted, pixels below are grey. The dashed black lines represent 90, 50, and 30% of the H_2 column density peak value derived from Herschel maps (Spezzano et al. 2016), 2.8×10^{22} cm^{-2}. The black triangle indicates the dust continuum peak (Ward-Thompson et al. 1999), and the white cross shows the c-C_3H_2 peak. The HPBW is indicated by a red circle in each panel. The dashed line in the *left panel* shows the cut used to produce Fig. 6.

10^6 years of cloud evolution, depending on the molecule. It is important to note that the emission of the different isotopologues of c-C_3H_2 across the core comes mostly from a layer of the core with a volume density that is similar to the critical density of the transitions (a few $\times 10^5$ cm^{-3}). We therefore only expect a minor variation of the $^{12}C/^{13}C$ ratio of c-C_3H_2 across L1544. While variations of the $^{12}C/^{13}C$ ratio with respect to the ISM value will affect the absolute values of the column densities and column density ratios we derive, they do not affect the overall morphology of the maps and the conclusions that we draw here.

The resulting deuterium fraction maps are shown in Fig. 2, where we show pixels with signal above 3σ. The dust continuum peak is indicated by a black triangle, and the white cross shows the c-C_3H_2 peak. The map of $R_{D/H}$(c-C_3H_2) = N(c-C_3HD)/N(c-C_3H_2) shows a peak located ~20″ east of the dust peak, reaching a maximum of 0.17 ± 0.01. In the map of $R_{D2/H2}$(c-C_3H_2) = N(c-C_3D_2)/N(c-C_3H_2), the peak is located ~20″ east of the dust peak, with a maximum of 0.025 ± 0.003. The level of deuteration in the map of $R_{D2/HD}$(c-C_3H_2) = N(c-C_3D_2)/N(c-C_3HD) ranges between 0.10 and 0.16, while the peak is located at the dust peak, with a maximum of 0.16 ± 0.03. The distribution shows a concentration of pixels with values of 0.15–0.16 spread between the dust peak and the c-C_3H_2 peak.

4.3. Non-LTE modelling

We tested the assumption of local thermodynamic equilibrium used in the derivation of the column densities by modelling the spectra at the dust peak using non-LTE simulations. To do this, we ran the radiative transfer codes RADEX (van der Tak et al. 2007) and MOLLIE (Keto 1990; Keto et al. 2004).

The radiative transfer code RADEX is one-dimensional and uses the escape probability formulation to simplify the calculations. For this work, we applied the geometry of a static, spherically symmetric, and uniform medium for the escape probability used to derive the column densities.

In contrast to RADEX, MOLLIE solves the radiative transfer equation on a three-dimensional grid using a spherically symmetric model of the source. This physical model is taken from Keto et al. (2015), who described an unstable quasi-equilibrium Bonnor-Ebert sphere with a peak central H_2 volume density of $n_0 \approx 10^7$ cm^{-3} and a central gas temperature of 6 K. The model provides the infall velocity, density, and gas temperature

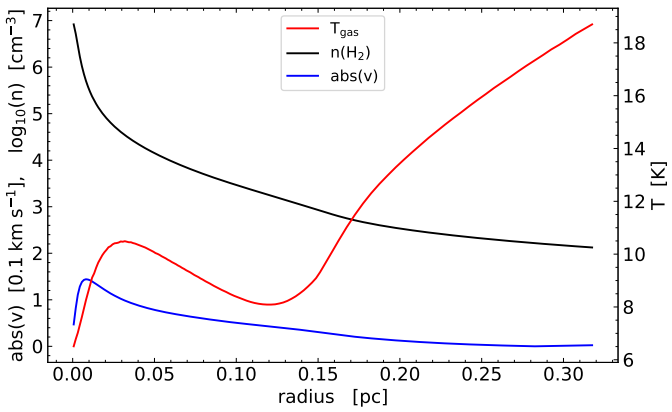

Fig. 3. Profiles of the gas temperature (red), H_2 number density (black, in logarithmic scale), and infall velocity (blue, in units of 0.1 km s^{-1}) for the L1544 model developed by Keto et al. (2015). The velocity in the model is negative, but here it is shown as positive for better readability.

structure for MOLLIE (see Fig. 3). The simulated molecular abundance profiles were derived using a state-of-the-art gas-grain chemical model (Sipilä et al. 2019), assuming an external visual extinction of A_V = 2 mag to account for the fact that L1544 is embedded in a molecular cloud. We employed the same initial abundances and chemical networks as in Sipilä et al. (2019). The initial abundances are reproduced here in Table 4. We assumed standard values for various model parameters; we set a constant cosmic-ray ionisation rate $\zeta = 1.3 \times 10^{-17}$ s^{-1}, a grain radius of 0.1 µm (monodisperse grains), and a grain material density of 2.5 g cm^{-3}. Redaelli et al. (2021) found a cosmic-ray ionisation rate of $\zeta = \sim 3 \times 10^{-17}$ s^{-1}, which is different by a factor of ~2 from the value we apply. In Appendix C, we discuss the effect of an increased cosmic-ray ionisation rate on the chemistry. The inital ortho-to-para ratio of H_2 was set to 10^{-3} and evolved with the rest of the chemistry. We adopted a two-phase description of gas-grain chemistry, that is, the ice on the grain surfaces was treated as a single reactive layer. Molecules may be desorbed thermally, or via cosmic-ray-induced desorption, photodesorption, or chemical desorption (with an efficiency of 1%).

Table 4. Initial abundances (with respect to $n_H \approx 2\,n(H_2)$) used in the chemical modelling.

Species	Abundance
H_2	5.00×10^{-1} [(a)]
He	9.00×10^{-2}
C^+	1.20×10^{-4}
N	7.60×10^{-5}
O	2.56×10^{-4}
S^+	8.00×10^{-8}
Si^+	8.00×10^{-9}
Na^+	2.00×10^{-9}
Mg^+	7.00×10^{-9}
Fe^+	3.00×10^{-9}
P^+	2.00×10^{-10}
Cl^+	1.00×10^{-9}
HD	1.60×10^{-5}

Notes. [(a)]The initial H_2 ortho-to-para ratio is 1×10^{-3}.

With the two different codes, we intend to test how a rather simple and often-used code such as RADEX, which only applies a general spherical core geometry with constant molecular abundance, volume density, and temperature, performs compared to a more sophisticated but time-consuming simulation such as MOLLIE, where the specific physical structure of a source and molecular abundance profiles across it are considered.

4.3.1. RADEX: Results

The results were obtained by manually fitting the synthetic spectra derived by RADEX to the observed spectra at the dust peak given in Fig. B.1. This was done using the CASSIS software (Vastel et al. 2015), assuming $n(H_2) = 10^6\,cm^{-3}$. We set T_{kin} = 5 K for c-C_3D_2 (3_{13}−2_{02}) and T_{kin} = 8 K for c-C_3H_2 (3_{22}−3_{13}) and c-C_3HD (3_{03}−2_{12}), corresponding to the lowest temperatures with available collision rates. The collision rates of c-C_3H_2, c-C_3HD, and c-C_3D_2 with H_2 were provided by Ben Khalifa et al. (2019) for the main species and by Ben Khalifa et al. (in prep.) for the isotopologues. Because of its different symmetry, the c-$H^{13}CC_2H$ isotopologue collisional rates cannot be deduced from the other rates, and they were not computed. Hence, we did not model the ^{13}C isotopologue in the non-LTE formalisms.

The total column densities corresponding to the best-fit solutions of RADEX are listed in Col. (2) of Table 5. The corresponding uncertainties of RADEX were estimated by varying the column density to result in a change of the peak temperature by 25%. To derive the total column densities of c-C_3H_2 and c-C_3D_2, the RADEX output column densities were multiplied by the ortho-to-para ratio, which is 3:1 and 1:2 for the two molecules, respectively. This was done because the collision rates used in the calculations treat ortho and para as two different species, so they were modelled separately.

Using RADEX, we can reproduce the column density of c-C_3H_2 observed at the dust peak within the error bars. The value for c-C_3HD is only slightly underestimated; c-C_3D_2, however, is overestimated by a factor of ∼2.

4.3.2. MOLLIE: Results

As output, MOLLIE produces a synthetic spectral line profile. The molecular column density was obtained by integrating the abundance profile multiplied by the gas density, and convolved to a desired beam size. The collisional coefficients needed for the line radiative transfer were provided by Ben Khalifa et al. (2019) and Ben Khalifa et al. (in prep.).

Table 5. Comparison of total column densities in units of $\times10^{12}\,cm^{-2}$.

Molecule	N(RADEX)	N_{t_1}(MOLLIE)	N_{t_2}(MOLLIE)
c-C_3H_2	14(4)	160	30
c-C_3HD	3.8(9)	3.8	0.8
c-C_3D_2	1.8(3)	0.79	0.23

Notes. The column densities derived with MOLLIE (N_M) are given at the chemical times $t_1 = 1.0\times10^5$ yr and $t_2 = 1.4\times10^5$ yr. The best fit for the deuterated species is t_1, and for the main species, it is t_2. The error on the derived values lies within a factor of 2.

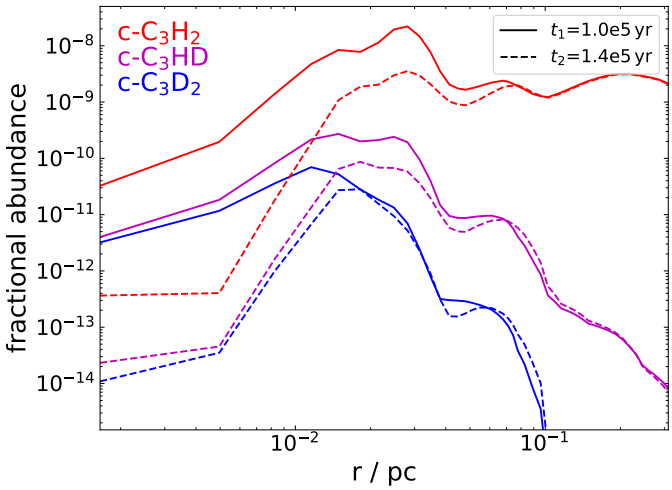

Fig. 4. Total molecular fractional abundance profiles with respect to H_2 used to obtain the MOLLIE best-fit solutions. c-C_3H_2 (red, c-C_3HD (pink) and c-C_3D_2 (blue) are plotted at two different time steps of the chemical model, $t_1 = 1.0\times10^5$ yr (solid lines) and $t_2 = 1.4\times10^5$ yr (dashed lines).

The total column densities corresponding to the best-fit solutions of MOLLIE are listed in Cols. 3 and 4 of Table 5. The values for c-C_3H_2 and c-C_3D_2 were derived by multiplying the MOLLIE output column densities by the ortho-to-para ratio (3:1 and 1:2 for c-C_3H_2 and c-C_3D_2, respectively) to account for the separate treatment of ortho and para species during the modelling. The errors of the column densities derived with MOLLIE lie roughly within a factor of 2, and are constrained by the resolution of the time steps of the chemical model.

Figure 4 shows the total molecular abundance profiles of c-C_3H_2, c-C_3HD and c-C_3D_2 with respect to H_2 at the two best-fitting time steps of the chemical model, $t_1 = 1.0\times10^5$ yr (solid lines) and $t_2 = 1.4\times10^5$ yr (dashed lines). At the first time step, c-C_3H_2 peaks at $\sim5\times10^3$ AU, while c-C_3HD and c-C_3D_2 peak at $\sim3\times10^3$ AU, slightly shifted towards the centre of the core. At the second time step, all peaks are shifted to larger radii because the molecules deplete in the centre of the core with evolving chemistry. Furthermore, c-C_3H_2 shows a rather flat profile in the outer radii and is also abundant in less dense parts, while the D-bearing species quickly drop off after they peak, staying more concentrated within the central parts.

We only varied the time step in the chemical model in our analysis, no other input parameters of the model. Therefore, we tested the effect of the various parameters by running four

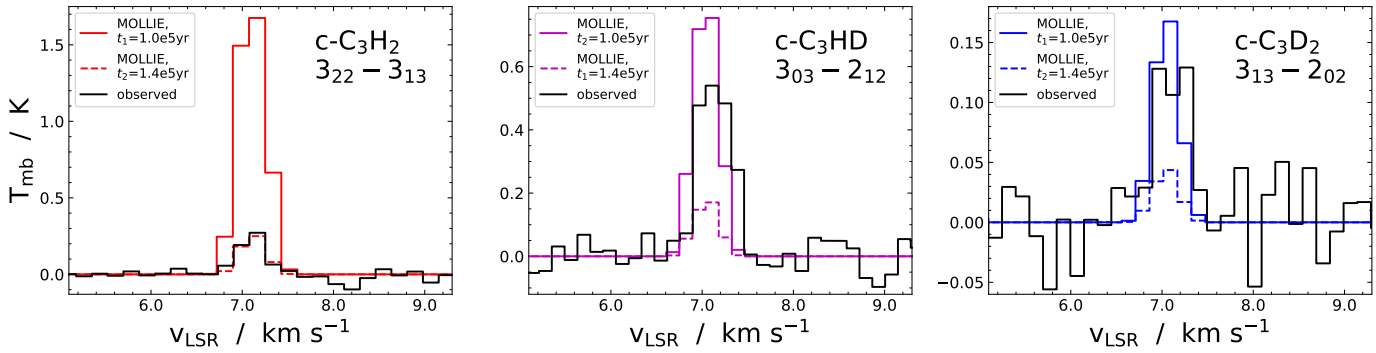

Fig. 5. Comparison of the best-fit solutions of spectra (coloured) modelled with MOLLIE at two different time steps of the chemical model, $t_1 = 1.0 \times 10^5$ yr (solid) and $t_2 = 1.4 \times 10^5$ yr (dashed), with the observed spectra (black). The synthetic spectra of c-C_3H_2 (*left*), c-C_3HD (*middle*), and c-C_3D_2 (*right*) are shown.

single-point simulations. The results of these test simulations are presented in Appendix C.

Figure 5 compares the spectra modelled with MOLLIE (coloured) at the two time steps $t_1 = 1.0 \times 10^5$ yr (solid lines) and $t_2 = 1.4 \times 10^5$ yr (dashed lines) with the observed spectra (black). The later time step shows a very good fit with the observed spectrum of c-C_3H_2. The deuterated isotopologues, on the other hand, are both underestimated by a factor of 3. They are better reproduced by t_1, where the main species is overestimated by a factor of 7. The same applies for the derived column densities; at t_2, the observed values of c-C_3HD and c-C_3D_2 are reproduced, while c-C_3H_2 is reproduced at t_1 within the error bars. One would expect the main species to match with the earlier time step, as the deuteration process is expected to occur late in the core evolution, with the deuterated isotopologues peaking at a later time. However, it is important to note that the chemical code used to produce the abundance profiles is static (i.e. the physical structure does not evolve with time). Thus, the time steps of the chemical model are not linked to the dynamical evolution of the cloud. This behaviour can be explained by the fact that the chemical timescale is approximately inversely proportional to the volume density (more reactants imply faster rates), so that the central regions have faster chemical timescales than the outer less dense regions. When a static core is used, this could lead to inconsistencies because in reality, a contracting core spends longer at low densities, while the denser regions only form at a later stage of its evolution. Therefore, the small difference between the time steps and the large difference between the resulting spectra demonstrates the sensitivity of the chemical model to the chosen time step and points out its limitations.

5. Discussion

The deuterium fraction maps presented in this work suggest that the deuteration of c-C_3H_2 is more efficient towards the centre of L1544. This implies that at high densities there is still c-C_3H_2 available to be deuterated, despite the freeze-out. However, carbon chains are not expected to trace the dense central regions of pre-stellar cores because they are expected to be frozen out. The detection of c-C_3D_2 peaking close to the dust peak demonstrates that a significant fraction of this species is still present towards the core centre. This might be due to the large amount of CO freeze-out, as our chemical models show that with increasing CO freeze-out, the formation of He^+ is enhanced. With increasing level of He^+ in the gas phase, the number of carbon atoms needed to produce carbon chains increases as well because He^+ efficiently destroys the CO molecules left in the gas phase via the reaction $He^+ + CO = C^+ + O + He$. This was already predicted by Ruffle et al. (1999), whose models show an increase of C^+ at 3×10^6 yr when CO starts its dramatic freeze-out, corresponding to a plateau in the HC_3N abundance (Figs. 1 and 2 in Ruffle et al. 1999)

The deuteration process of c-C_3H_2 consists of two reactions, the proton-deuteron transfer with H_2D^+ and the subsequent dissociative recombination with electrons (see Spezzano et al. 2013). Therefore, the D/H ratio of c-C_3H_2 is directly related to that of H_3^+. The distribution of H_2D^+ across L1544 was shown to be extended and an excellent tracer of the dust continuum (Vastel et al. 2006; Koumpia et al. 2020), with the emission peak at the dust peak. The correlation between the degree of deuteration in molecules and the abundance of H_2D^+ found by Vastel et al. (2006) is now further confirmed by our map of c-C_3D_2.

The deuterium fraction maps of c-C_3H_2 reveal how the efficiency of the deuteration varies across the core. However, it has to be taken into account that the deuterated isotopologues are much less abundant at larger radii than the main species, and they are more concentrated at higher densities (see the abundance profiles in Fig. 4). Therefore, the column density of the normal species also contains contributions from the outer layers of the core, where c-C_3H_2 is still abundant, while c-C_3HD and c-C_3D_2 are not present. The observed emission of the normal isotopologue therefore does not necessarily come from the same layers in which the deuterated isotopologues are located, and the corresponding deuterium fraction maps have to be interpreted with caution. By analysing $R_{D2/HD}$(c-C_3H_2), this problem is avoided because the two molecules are expected to trace more similar regions of the core (as also shown by the abundace profiles in Fig. 4). The $R_{D2/HD}$(c-C_3H_2) map shows a peak slightly shifted to the south-east of the dust peak, in between the dust and c-C_3H_2 peaks. This confirms that the deuteration process, and especially higher-order deuteration, is more efficient towards the centre of the core. The peak values of the deuteration maps derived in this work are $R_{HD/H2}$(c-C_3H_2) = 0.17, $R_{D2/H2}$(c-C_3H_2) = 0.025, and $R_{D2/HD}$(c-C_3H_2) = 0.16, in good agreement with previous measurements towards the dust peak of L1544 (see e.g. Spezzano et al. 2013, Chantzos et al. 2018).

Using the non-LTE models RADEX and MOLLIE, we were able to reproduce the observed spectra towards the dust peak of L1544 in both cases. The derived column densities agree with the LTE calculations within a factor of 2. This shows that for our observed transitions, we can safely use RADEX for non-LTE calculations instead of a costly and time-consuming simulation

such as MOLLIE. We further used the results of RADEX and MOLLIE to estimate the optical depth of the possibly optically thick transition of c-C_3H_2, (3_{22}−3_{13}). We found values ranging from 0.07 up to 0.3, indicating optically thin emission. Nevertheless, the non-LTE simulations confirm that the assumption of CTex is a useful approximation to derive the column density of optically thin lines.

Recently, Redaelli et al. (2019) and Chacón-Tanarro et al. (2019) studied the deuteration throughout L1544 using emission maps of the molecules N_2H^+, HCO^+ and CH_3OH, H_2CO, respectively. The molecules discussed in Redaelli et al. (2019), N_2H^+ and HCO^+, show a similar behaviour to c-C_3H_2: the D-bearing species peak closer to the dust peak than their corresponding normal species, and the deuteration maps show a compact morphology around the dust peak. N_2H^+ is more deuterated than c-C_3H_2, as N_2, and therefore N_2H^+, is a late-type molecule and is less depleted in the dense central parts of the core. Thus, N_2H^+ reaches higher levels of deuteration (26%) than c-C_3H_2 (17%), tracing the densest regions. HCO^+, on the other hand, is formed from CO, which is highly depleted in the centre. It therefore traces outer layers of the core, similar to c-C_3H_2, but shows low levels of deuteration (≈3.5%).

Using methanol (CH_3OH) and formaldehyde (H_2CO), which form on dust grain surfaces, Chacón-Tanarro et al. (2019) focused on the deuteration process in the solid phase. A comparison of the deuteration maps of methanol to the $R_{HD/H2}$(c-C_3H_2) map and the $R_{D2/H2}$(c-C_3H_2) map shows an interesting similarity. The deuteration peaks of both molecules are shifted from the dust peak towards the opposite direction of their respective molecular peaks with respect to the major axis of L1544. Following this, the morphology of the maps might not be the consequence of an increased deuteration, but rather a steep decrease of the column density of the main species in the outer layers of the core. The emission of the deuterated isotopologues instead only comes from the inner layers and is not affected by the inhomogeneous interstellar radiation field around the core (which drives the segregation among methanol and c-C_3H_2). This is confirmed by the fact that the $R_{D2/HD}$(c-C_3H_2) ratio peaks just next to the dust peak. The distribution of the deuterium fraction of H_2CO shows an opposite behaviour with respect to c-C_3H_2. The $R_{HD/H2}$(c-C_3H_2) map is extended through the core, while for $R_{HD/H2}$(H_2CO), the map is more centred around its peak located towards the north-west of the dust peak. For the double-deuteration maps the same applies, but this time, the distribution of H_2CO is more extended and c-C_3H_2 is more centred. The more extended $R_{D2/H2}$(H_2CO) map might be linked to the fact that the H_2CO isotopologues have both grain-surface and gas-phase formation mechanisms, while c-C_3H_2 isotopologues solely form in the gas phase. The $R_{D2/HD}$(H_2CO) map is not discussed in Chacón-Tanarro et al. (2019) due to high uncertainties and hence cannot be used for a comparison. A major difference between c-C_3H_2 and H_2CO is their deuteration level. For H_2CO, both $R_{HD/H2}$(H_2CO) and $R_{D2/H2}$(H_2CO) lie below 0.05. In contrast to this, for c-C_3H_2, the singly deuterated species is much more abundant than the doubly deuterated one, reaching $R_{HD/H2}$(c-C_3H_2) = 0.17 and $R_{D2/H2}$(c-C_3H_2) = 0.025, respectively. This indicates that for H_2CO, higher-order deuteration occurs much more efficiently.

By cutting across the dust peak and the $R_{HD/H2}$(HCO^+) maximum, Redaelli et al. (2019) compared the trends of the deuteration maps of their molecular tracers. Figure 6 applies the same cut to the deuteration maps of c-C_3H_2 derived in this work, plotting the deuteration fractions as a function of the impact parameter (projected distance to the dust peak) and comparing

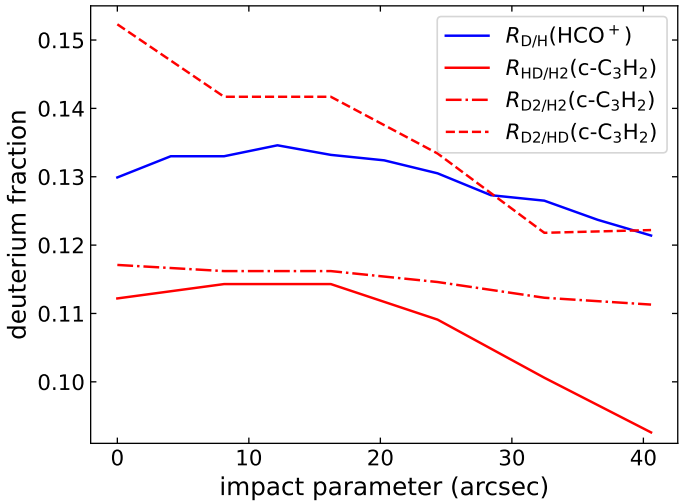

Fig. 6. Comparison of the trends of the HCO^+ deuteration map presented in Redaelli et al. (2019) and the deuteration maps of c-C_3H_2 derived in this work along the cut shown in Fig. 10 in Redaelli et al. (2019). The data points of $R_{HD/H2}$(HCO^+) and $R_{D2/H2}$(c-C_3H_2) are shifted upwards by 0.10 to facilitate comparison.

them to HCO^+. The cut is visualised as a dashed line in the left panel of Fig. 2. Along the cut, the deuteration levels of $R_{HD/H2}$(c-C_3H_2) and $R_{D2/HD}$(c-C_3H_2) decrease faster than $R_{D2/H2}$(c-C_3H_2) and $R_{HD/H2}$(HCO^+). The slope of $R_{HD/H2}$(c-C_3H_2) shows a similar behaviour as HCO^+, as both peak between 10″–20″ from the dust peak and then drop off, although the drop of c-C_3H_2 is steeper. The fast decrease of $R_{D2/HD}$(c-C_3H_2) with increasing distance from the dust peak confirms once more that the deuteration process is most efficient in the central region. This enhanced c-C_3H_2 deuteration towards the centre of a pre-stellar core could explain the high $R_{HD/H2}$(c-C_3H_2) values found by Chantzos et al. (2018) towards the protostar HH211, one of the youngest class 0 sources.

6. Conclusions

We studied the deuteration process of cyclopropenylidene towards the pre-stellar core L1544. We presented the first emission map of doubly deuterated c-C_3H_2, along with the emission maps of its singly deuterated and non-deuterated isotopologues. Peaking at the centre of the core, the column density map of c-C_3D_2 proves that carbon-chain molecules are still present at the high central densities. This is possible due to an increased abundance of He^+ that destroys CO molecules and therefore increases the number of free carbon atoms available to form c-C_3H_2 (Ruffle et al. 1999). Furthermore, the distributions of c-C_3HD and c-C_3D_2 indicate that the deuterated forms of c-C_3H_2 are preferentially located towards the centre of L1544, where the increased abundance of H_2D^+ drives the deuteration process, and do not trace the c-C_3H_2 peak located in the south-east, which is caused by external illumination of the interstellar radiation field. Using the column density maps calculated assuming CTex, we derived the first deuteration maps of c-C_3H_2. Showing a maximum at the dust peak, the maps confirm that the deuteration process of c-C_3H_2 is more efficient towards the centre of the core. The maximum values in the maps are $R_{HD/H2}$(c-C_3H_2) = 0.17 ± 0.01, $R_{D2/H2}$(c-C_3H_2) = 0.025 ± 0.003, and $R_{D2/HD}$(c-C_3H_2) = 0.16 ± 0.03, which agree

well with previous single-pointing measurements (Spezzano et al. 2013; Chantzos et al. 2018).

Using the non-LTE radiative transfer models RADEX and MOLLIE, we were able to reproduce the spectra of c-C_3H_2, c-C_3HD and c-C_3D_2 at the dust peak of L1544. The derived non-LTE column densities agree with the CTex calculations within a factor of 2. The comparison of our methods shows that for our observed transitions, we can safely use RADEX for non-LTE calculations instead of a time-consuming simulation such as MOLLIE.

Finally, we compared the deuterium fraction maps derived in this work to the deuteration of other molecular tracers. The discussion showed that studying the deuteration of different species can bring important information about the chemistry of different parts of the source and helps to build a comprehensive picture of L1544. However, only a limited number of deuteration maps is available in the literature so far. Future projects will be able to address this deficit and lead to a deeper understanding of the deuteration process of individual molecules. In particular, future studies can further investigate the detection of carbon-chain molecules at unexpectedly high densities to place tighter constraints on gas-grain chemical models. Suitable candidates for observations of other abundant carbon-chains are for example CH_3CCH and HC_3N, which show a segregation towards the pre-stellar core L1544 that is not yet understood (see Spezzano et al. 2017).

Acknowledgements. The authors wish to thank the anonymous referee for useful comments. S.S. and K.G. wish to thank the Max Planck Society for the Max Planck Research Group funding. All others authors affiliated to the MPE wish to thank the Max Planck Society for financial support.

References

Bacmann, A., Lefloch, B., Ceccarelli, C., et al. 2003, ApJ, 585, L55
Ben Khalifa, M., Sahnoun, E., Wiesenfeld, L., et al. 2019, Phys. Chem. Chem. Phys., 21, 1443
Bogey, M., Demuynck, C., Destombes, J. L., & Dubus, H. 1987, J. Mol. Spectr., 122, 313
Caselli, P., Walmsley, C. M., Tafalla, M., Dore, L., & Myers, P. C. 1999, ApJ, 523, L165
Caselli, P., Keto, E., Bergin, E. A., et al. 2012, ApJ, 759, L37
Caselli, P., Walmsley, C. M., Zucconi, A., et al. 2002a, ApJ, 565, 331
Caselli, P., Walmsley, C. M., Zucconi, A., et al. 2002b, ApJ, 565, 344
Caselli, P., Pineda, J. E., Zhao, B., et al. 2019, ApJ, 874, 89
Ceccarelli, C., Caselli, P., Bockelée-Morvan, D., et al. 2014, in Protostars and Planets VI, eds. H. Beuther, R. S. Klessen, C. P. Dullemond, & T. Henning (Tucson: University of Arizona Press), 859
Chacón-Tanarro, A., Caselli, P., Bizzocchi, L., et al. 2019, A&A, 622, A141
Chantzos, J., Spezzano, S., Caselli, P., et al. 2018, ApJ, 863, 126
Colzi, L., Sipilä, O., Roueff, E., Caselli, P., & Fontani, F. 2020, A&A, 640, A51
Cox, P., Guesten, R., & Henkel, C. 1987, A&A, 181, L19
Crapsi, A., Caselli, P., Walmsley, C. M., et al. 2005, ApJ, 619, 379
Crapsi, A., Caselli, P., Walmsley, M. C., & Tafalla, M. 2007, A&A, 470, 221
Dalgarno, A., & Lepp, S. 1984, ApJ, 287, L47
Galli, P. A. B., Loinard, L., Bouy, H., et al. 2019, A&A, 630, A137
Gerin, M., Wootten, H. A., Combes, F., et al. 1987, A&A, 173, L1
Hily-Blant, P., Faure, A., Rist, C., Pineau des Forêts, G., & Flower, D. R. 2018, MNRAS, 477, 4454
Keto, E. R. 1990, ApJ, 355, 190
Keto, E., & Caselli, P. 2010, MNRAS, 402, 1625
Keto, E., Rybicki, G. B., Bergin, E. A., & Plume, R. 2004, ApJ, 613, 355
Keto, E., Caselli, P., & Rawlings, J. 2015, MNRAS, 446, 3731
Kong, S., Caselli, P., Tan, J. C., Wakelam, V., & Sipilä, O. 2015, ApJ, 804, 98
Koumpia, E., Evans, L., Di Francesco, J., van der Tak, F. F. S., & Oudmaijer, R. D. 2020, A&A, 643, A61
Lee, C. W., Myers, P. C., & Tafalla, M. 2001, ApJS, 136, 703
Lucas, R., & Liszt, H. S. 2000, A&A, 358, 1069
Madden, S. C., Irvine, W. M., Matthews, H. E., Friberg, P., & Swade, D. A. 1989, AJ, 97, 1403
Majumdar, L., Gratier, P., Andron, I., Wakelam, V., & Caux, E. 2017, MNRAS, 467, 3525
Mangum, J. G., & Shirley, Y. L. 2015, PASP, 127, 266
Matthews, H. E., & Irvine, W. M. 1985, ApJ, 298, L61
Milam, S. N., Savage, C., Brewster, M. A., Ziurys, L. M., & Wyckoff, S. 2005, ApJ, 634, 1126
Müller, H. S. P., Thorwirth, S., Roth, D. A., & Winnewisser, G. 2001, A&A, 370, L49
Ohashi, N., Lee, S. W., Wilner, D. J., & Hayashi, M. 1999, ApJ, 518, L41
Pagani, L., Salez, M., & Wannier, P. G. 1992, A&A, 258, 479
Park, I. H., Wakelam, V., & Herbst, E. 2006, A&A, 449, 631
Pety, J. 2005, in SF2A-2005: Semaine de l'Astrophysique Francaise, eds. F. Casoli, T. Contini, J. M. Hameury, & L. Pagani, 721
Qi, C., Öberg, K. I., Wilner, D. J., & Rosenfeld, K. A. 2013, ApJ, 765, L14
Redaelli, E., Bizzocchi, L., Caselli, P., et al. 2019, A&A, 629, A15
Redaelli, E., Sipilä, O., Padovani, M., et al. 2021, A&A, 656, A109
Ruffle, D. P., Hartquist, T. W., Caselli, P., & Williams, D. A. 1999, MNRAS, 306, 691
Seaquist, E. R., & Bell, M. B. 1986, ApJ, 303, L67
Sipilä, O., Caselli, P., Redaelli, E., Juvela, M., & Bizzocchi, L. 2019, MNRAS, 487, 1269
Spezzano, S., Tamassia, F., Thorwirth, S., et al. 2012, ApJS, 200, 1
Spezzano, S., Brünken, S., Schilke, P., et al. 2013, ApJ, 769, L19
Spezzano, S., Bizzocchi, L., Caselli, P., Harju, J., & Brünken, S. 2016, A&A, 592, L11
Spezzano, S., Caselli, P., Bizzocchi, L., Giuliano, B. M., & Lattanzi, V. 2017, A&A, 606, A82
Teyssier, D., Hily-Blant, P., Gerin, M., et al. 2005, ESA SP, 577, 423
Thaddeus, P., Guelin, M., & Linke, R. A. 1981, ApJ, 246, L41
Thaddeus, P., Vrtilek, J. M., & Gottlieb, C. A. 1985, ApJ, 299, L63
van der Tak, F. F. S., Black, J. H., Schöier, F. L., Jansen, D. J., & van Dishoeck, E. F. 2007, A&A, 468, 627
Vastel, C., Caselli, P., Ceccarelli, C., et al. 2006, ApJ, 645, 1198
Vastel, C., Bottinelli, S., Caux, E., Glorian, J. M., & Boiziot, M. 2015, in SF2A-2015: Proceedings of the Annual meeting of the French Society of Astronomy and Astrophysics, 313
Vrtilek, J. M., Gottlieb, C. A., & Thaddeus, P. 1987, ApJ, 314, 716
Ward-Thompson, D., Motte, F., & Andre, P. 1999, MNRAS, 305, 143
Willacy, K., Langer, W. D., & Velusamy, T. 1998, ApJ, 507, L171
Williams, J. P., Myers, P. C., Wilner, D. J., & Di Francesco, J. 1999, ApJ, 513, L61

Appendix A: Column density maps

In Figure A.1 we show the derived column density maps of the observed molecules using the parameters listed in Table 2.

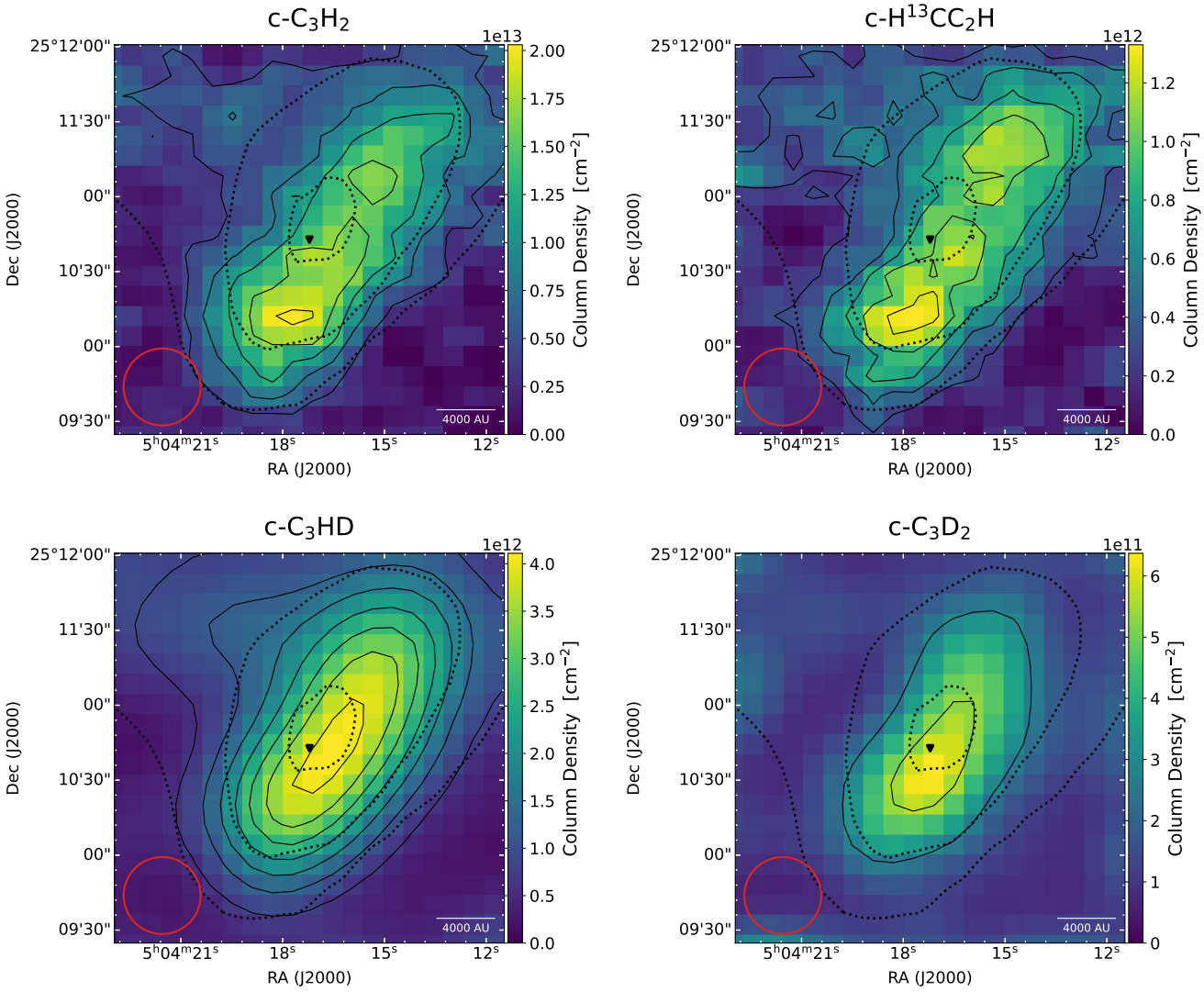

Fig. A.1. Column density maps of the molecules we used to calculate the deuteration fraction maps. The dashed black lines represent 90%, 50%, and 30% of the H_2 column density peak value derived from *Herschel* maps (Spezzano et al. 2016), 2.8×10^{22} cm^{-2}. The solid lines represent contours of the column density, starting at 3σ with steps of 3σ. *From top to bottom and left to right*, the average errors on the column density are 1×10^{12}, 9×10^{10}, 2×10^{11} and 1×10^{11} in units of cm^{-2}. The dust peak is indicated by the black triangle. The beam size of the 30 m telescope, HPBW = 31″, is shown by the red circle, and the scale bar is shown in the bottom right corners.

Appendix B: Averaged spectra

Figure B.1 shows the spectra extracted at the dust peak (Ward-Thompson et al. 1999) and the c-C_3H_2 peak (Spezzano et al. 2016) of L1544. Fitted Gaussian profiles are overlaid (red).

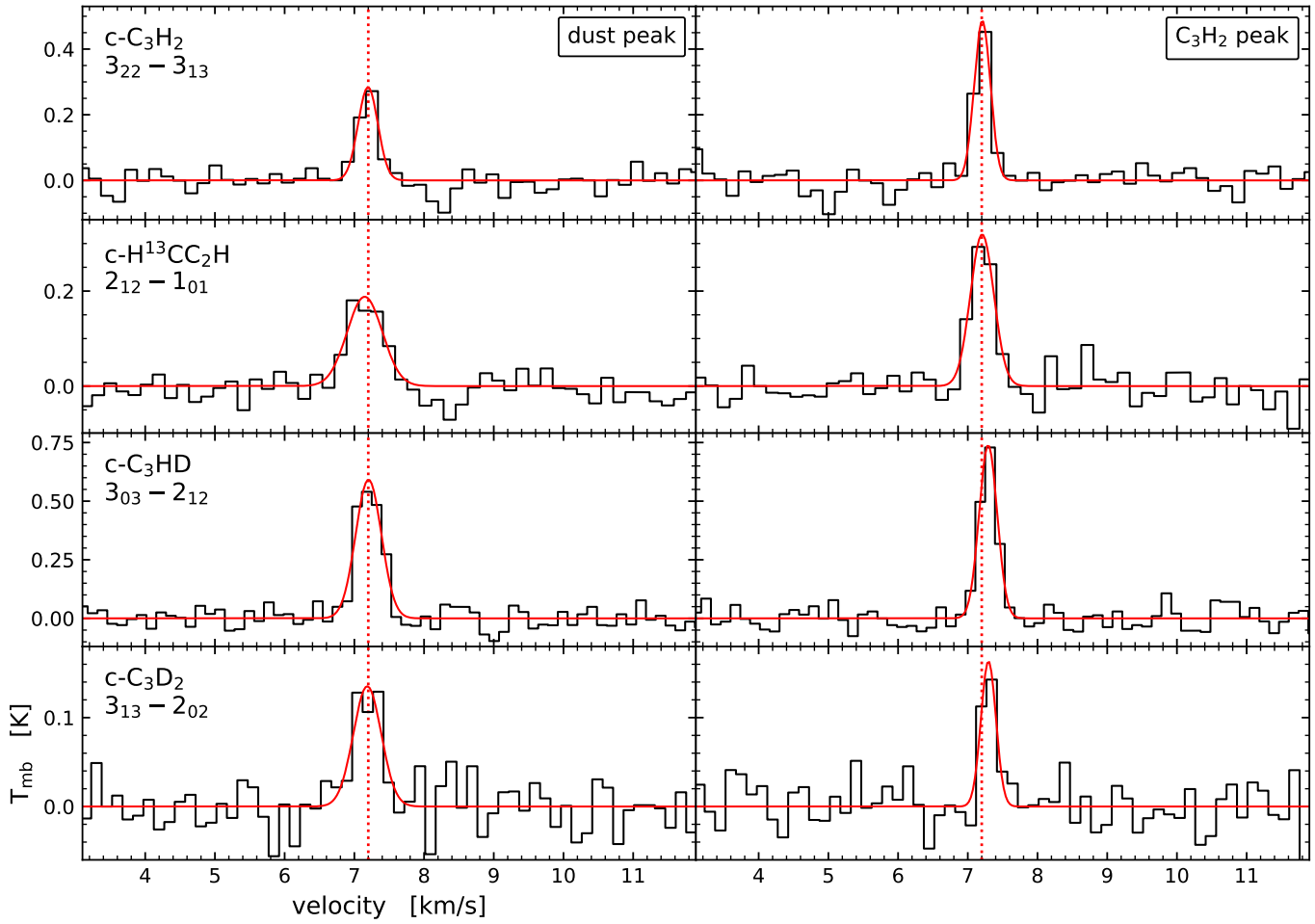

Fig. B.1. Comparison of extracted spectra (black) of the transitions listed in Table 1 at the dust peak (*left*) and the c-C_3H_2 peak (*right*) of L1544. The fitted Gaussian profiles are overlaid (red). The vertical lines indicate the systemic velocity of the source, 7.2 km s^{-1}.

Appendix C: Variation of input parameters of the chemical model

To test the effect of the various parameters, we ran four single-point simulations, assuming physical conditions roughly representative of the outer core region where the c-C_3H_2 abundance peaks: $n(H_2) = 10^4$ cm^{-3}, $T = 10$ K, and $A_V = 5$ mag. In addition to the fiducial parameter set, we tested three variations with respect to the fiducial model: 1) decreased C/O ratio (from ∼.47 to ∼.35), 2) higher cosmic-ray ionisation rate ($\zeta = 10^{-16}$ s^{-1}), and 3) higher initial H_2 ortho-to-para ratio (3). Figure C.1 shows the resulting D/H ratios as a function of time in these four cases. The solid lines represent the fiducial case, and the dashed, dotted, and dash-dotted lines represent cases 1 to 3, respectively, as defined above.

A variation in the applied C/O ratio from ∼0.47 down to ∼0.35 changes the results only slightly. An increase in the initial ortho-to-para ratio of H_2 up to o:p = 3 simply delays the evolution of the D/H ratios, eventually arriving at the same end result as the in the case of a low initial ratio. This behaviour was also observed by Kong et al. (2015). Only the cosmic-ray ionisation rate seems to have a larger effect, where an increase up to 10^{-16} s^{-1} reduces both D/H ratios. Redaelli et al. (2021) previously found the ionisation rate to be $\sim 3 \times 10^{-17}$ s^{-1}, which is different by less than a factor of 3 from our fiducial value. The test simulations show that the time is not the only variable that influences the D/H ratios of c-C_3H_2. While we only explored a small part of the parameter space and the tests were limited to a single point and cannot be used to conclude about the column densities, we do not expect variations of more than a factor of a few in the c-C_3H_2 D/H ratios as long as the model parameters remain reasonably close to those in the fiducial model. A complete parameter-space exploration is beyond the scope of the present work.

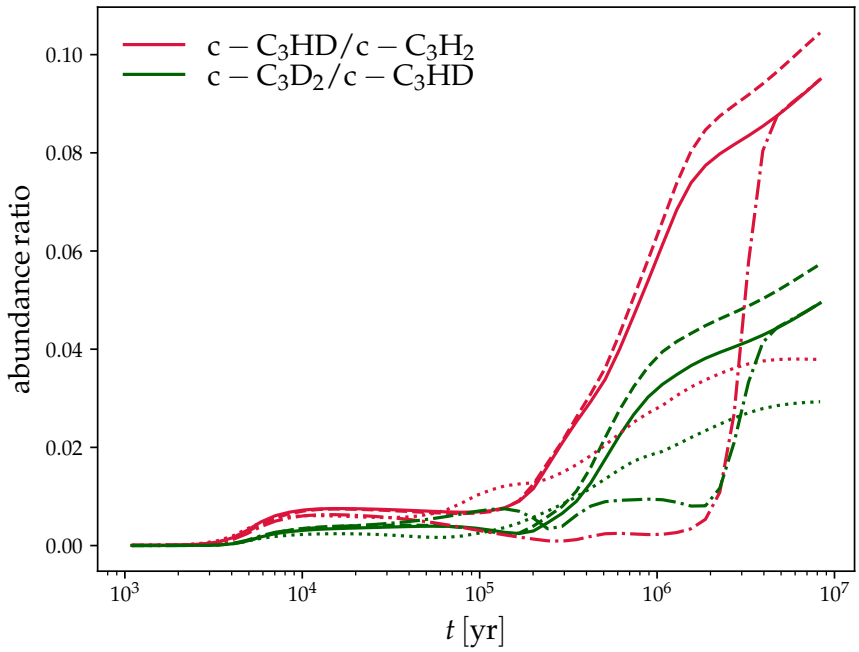

Fig. C.1. Comparison of the evolution of the D/H ratios of c-C_3H_2 with varied input parameters in the chemical model: fiducial model (solid lines), decreased C/O ratio (dashed lines), higher CR ionisation rate (dotted lines), and higher initial H_2 ortho-to-para ratio (dash-dotted lines).